Journal of Fluids and Structures (2002) **16**(4), 497–527
doi:10.1006/jfls.2000.0434, available online at http://www.idealibrary.com on IDEAL®

DEVELOPMENT OF A THREE-DIMENSIONAL VISCOUS AEROELASTIC SOLVER FOR NONLINEAR PANEL FLUTTER

R. E. GORDNIER and M. R. VISBAL

Air Force Research Laboratory, Wright-Patterson AFB, OH 45433-7913, U.S.A.

(Received 11 August 2000, and in final form 29 August 2001)

A new three-dimensional (3-D) viscous aeroelastic solver for nonlinear panel flutter is developed in this paper. A well-validated full Navier–Stokes code is coupled with a finite-difference procedure for the von Karman plate equations. A subiteration strategy is employed to eliminate lagging errors between the fluid and structural solvers. This approach eliminates the need for the development of a specialized, tightly coupled algorithm for the fluid/structure interaction problem. The new computational scheme is applied to the solution of inviscid two-dimensional panel flutter problems for subsonic and supersonic Mach numbers. Supersonic results are shown to be consistent with the work of previous researchers. Multiple solutions at subsonic Mach numbers are discussed. Viscous effects are shown to raise the flutter dynamic pressure for the supersonic case. For the subsonic viscous case, a different type of flutter behavior occurs for the downward deflected solution with oscillations occurring about a mean deflected position of the panel. This flutter phenomenon results from a true fluid/structure interaction between the flexible panel and the viscous flow above the surface. Initial computations have also been performed for inviscid, 3-D panel flutter for both supersonic and subsonic Mach numbers.

1. INTRODUCTION

THE PROBLEM OF PANEL FLUTTER has been the subject of extensive investigation for a number of years. The majority of the work to date has considered only simple linear aerodynamic models (e.g., Dowell 1966, 1967, 1970; Adbel-Motaglay, Chen & Mei 1999). Recently, Davis and Bendiksen (Davis & Bendiksen 1993; Davis 1994; Bendiksen & Davis 1995) have employed an improved modelling of the aerodynamics by tightly coupling the Euler equations with a nonlinear finite-element model for two-dimensional (2-D), transonic panel flutter problems. This paper describes the development of a three-dimensional (3-D) aeroelastic solver for nonlinear panel flutter. The approach couples a full Navier–Stokes solver with a finite-difference code for the von Karman plate equations. The present effort extends the preliminary work of Selvam, Visbal & Morton 1998 for 2-D panel flutter.

Historically, researchers interested in dynamic aeroelastic computations have taken well-validated, implicit Navier–Stokes algorithms developed to solve complex flows over 3-D, rigid bodies, and extended them to include aeroelastic effects. The most common practice is to simply lag the effects of moving/deforming structures by one time step [Guruswamy 1990; Morton & Beran 1995), allowing current algorithms to be used in updating the aerodynamic variables. Bendiksen & Hwang (1997) point out that when taking this approach unknown phase and integration errors are introduced leading, in some cases, to incorrect prediction of the stability behavior of the fluid–structural system. To

0889–9746/02/040497 + 31 $35.00/0

overcome this problem, Davis and Bendiksen (Davis & Bendiksen 1993; Davis 1994) take the alternate approach of developing a new tightly integrated algorithm in which the fluid and structure are modelled as a single dynamical system. Although this approach has been shown to eliminate the lagging errors, it requires the development of an entirely new solver.

An attractive alternate method of eliminating these phase and integration errors, while utilizing existing fluid dynamic and structural dynamic algorithms, is implementing Newton-like subiterations (Rizzetta & Visbal 1992; Morton, Melville & Visbal 1997). Subiterations can eliminate errors from linearization and factorization, as well as from lagged boundary conditions and turbulence models. The result is a fully implicit coupling between the fluid and structures without having to develop a completely new tightly coupled solver. Melville, Morton & Rizzeta (1997) have used this technique to couple a 3-D Navier–Stokes code with a general, linear second-order structural model. This solver has been applied successfully to the problems of transonic wing flutter [Gordnier & Melville 1998), tail-buffet (Morton, Rizzetta & Melville 1998) and limit-cycle oscillations (Gordnier & Melville 1999).

In the present work, the interest is in developing a solver that considers both nonlinear structures and aerodynamics. To this end, the linear structural model employed by Melville *et al.* is replaced by a finite-difference solution procedure for the 3-D, nonlinear, von Karman plate equations. The Newmark-β method is used for the time integration of these equations. This demonstrates the ability of the subiteration strategy to couple disparate time integration schemes for the fluid and structural solvers.

Several classical plate problems are computed to validate the von Karman plate solver. The new coupled code is then applied to the solution of 2-D and 3-D panel flutter problems from transonic to supersonic flow. Both inviscid (Euler) and viscous (Navier–Stokes) aerodynamic models are considered. Interesting new panel flutter phenomena that result from the inclusion of viscous flow effects are described. These results highlight the importance of incorporating high fidelity models for both fluids and structures.

2. GOVERNING EQUATIONS

2.1. Aerodynamic Governing Equations

The aerodynamic governing equations are the unsteady, compressible, 3-D Navier–Stokes equations written in nondimensional, strong-conservation law form (Pulliam & Steger 1980) employing a general time-dependent transformation. The resulting system of governing equations is expressed as

$$\frac{\partial \hat{U}}{\partial t} + \frac{\partial}{\partial \xi}\left(\hat{F} - \frac{1}{\mathrm{Re}}\hat{F}_v\right) + \frac{\partial}{\partial \eta}\left(\hat{G} - \frac{1}{Re}\hat{G}_v\right) + \frac{\partial}{\partial \zeta}\left(\hat{H} - \frac{1}{Re}\hat{H}_v\right) = 0. \tag{1}$$

With this formulation, the vector of dependent variables $\hat{U}$ is given as

$$\hat{U} = \frac{1}{J}U = \frac{1}{J}[\rho, \quad \rho u, \quad \rho v, \quad \rho w, \quad \rho E]^{\mathrm{T}}. \tag{2}$$

All variables have been normalized by the appropriate combination of freestream density, velocity and a characteristic length. Sutherland's law for the molecular viscosity coefficient μ and the perfect gas relationship are also employed, and Stokes' hypothesis for the bulk viscosity coefficient is assumed.

2.2. Structural Dynamics Governing Equations

The governing structural equations are the von Karman equations which are required for large plate deflections. Derivations for these equations may be found in a number of sources, including Fung (1965). For the von Karman theory, the plate is assumed to be isotropic, of uniform small thickness and initially flat. The normal deflection of the plate is assumed to be of the order of the thickness of the plate, while the tangential displacements are assumed infinitesimal. Finally, Kirchoff's hypothesis is employed with tractions on surfaces parallel to the middle surface assumed negligible and strains varying linearly with the plate thickness.

Using these assumptions, the governing equations for the plate motion may be written in nondimensional form as

$$\frac{\lambda}{\mu_s}\frac{\partial^2 \delta w}{\partial t^2} + \nabla^4 \delta w - N''_x \frac{\partial^2 \delta w}{\partial x^2} - 2{\cdot}0 N''_{xy} \frac{\partial^2 \delta w}{\partial x \partial y} - N''_y \frac{\partial^2 \delta w}{\partial y^2}$$

$$= \frac{\lambda}{h}\left[S_{zz}\left(\frac{h}{2}\right) - S_{zz}\left(-\frac{h}{2}\right)\right] + \frac{\lambda}{h}\left[\frac{\partial m'_x}{\partial x} + \frac{\partial m'_y}{\partial y}\right], \tag{3}$$

$$\frac{\partial N'_x}{\partial x} + \frac{\partial N'_{xy}}{\partial y} + f'_x = 0, \tag{4}$$

$$\frac{\partial N'_{xy}}{\partial x} + \frac{\partial N'_y}{\partial y} + f'_y = 0, \tag{5}$$

where

$$N''_x = \lambda N'_x = 12{\cdot}0\left(\frac{\partial \delta u}{\partial x} + \nu \frac{\partial \delta v}{\partial y} + \frac{1}{2}\left[\left(\frac{\partial \delta w}{\partial x}\right)^2 + \nu\left(\frac{\partial \delta w}{\partial y}\right)^2\right]\right), \tag{6}$$

$$N''_y = \lambda N'_y = 12{\cdot}0\left(\frac{\partial \delta v}{\partial y} + \nu \frac{\partial \delta u}{\partial x} + \frac{1}{2}\left[\left(\frac{\partial \delta w}{\partial y}\right)^2 + \nu\left(\frac{\partial \delta w}{\partial x}\right)^2\right]\right), \tag{7}$$

$$N''_{xy} = \lambda N'_{xy} = 12{\cdot}0\,\frac{1-\nu}{2}\left(\frac{\partial \delta u}{\partial y} + \frac{\partial \delta v}{\partial x} + \frac{\partial \delta w}{\partial x}\frac{\partial \delta w}{\partial y}\right), \tag{8}$$

$$f'_x = S_{zx}\left(\frac{h}{2}\right) - S_{zx}\left(-\frac{h}{2}\right), \qquad f'_y = S_{zy}\left(\frac{h}{2}\right) - S_{zy}\left(-\frac{h}{2}\right), \tag{9, 10}$$

$$m'_x = \frac{h}{2}\left[S_{zx}\left(\frac{h}{2}\right) + S_{zx}\left(-\frac{h}{2}\right)\right], \qquad m'_y = \frac{h}{2}\left[S_{zy}\left(\frac{h}{2}\right) + S_{zy}\left(-\frac{h}{2}\right)\right]. \tag{11, 12}$$

These equations are written in a Lagrangian reference frame, where x, y and z refer to the original undeflected plate location and δu, δv and δw are the corresponding displacements from the undeflected position. The equations have been nondimensionalized based on the freestream density, freestream velocity and the length of the plate. In addition, the nondimensional displacements δu and δv have been scaled by the square of the nondimensional plate thickness, h^2. Similarly, δw has been scaled by the nondimensional plate thickness, h. The terms S_{zx}, S_{zy} and S_{zz} are elements of the Kirchoff stress tensor.

Equations (3)–(5) are a coupled set of nonlinear equations for the plate deflections. The nonlinear terms in equation (3) arise due to the stretching of the middle surface of the plate resulting in the development of the membrane stresses N'_x, N'_y, and N'_{xy}.

3. NUMERICAL PROCEDURE

3.1. Aerodynamic Solver

Solutions to equation (1) are obtained numerically using the implicit approximately factored finite-difference algorithm of Beam & Warming (1978), employing a Newton-like subiteration procedure (Gordnier & Visbal 1991). The numerical algorithm is obtained by utilizing either a two- or three-point backward time differencing and linearizing about the solution at subiteration level p. Either first- or second-order temporal accuracy can be prescribed in this iterative approach by specifying $\phi = 0$ or $\phi = \frac{1}{2}$, respectively, in equation (13). The numerical algorithm is written in approximately factored, delta form as

$$\left[J^{-1^{p+1}} + \phi^i \Delta t_s \delta_\xi \left(\frac{\partial \hat{F}^p}{\partial U} - \frac{1}{\mathrm{Re}} \frac{\partial \hat{F}_v^p}{\partial U}\right)\right] J^{p+1}$$

$$\times \left[J^{-1^{p+1}} + \phi^i \Delta t_s \delta_\eta \left(\frac{\partial \hat{G}^p}{\partial U} - \frac{1}{\mathrm{Re}} \frac{\partial \hat{G}_v^p}{\partial U}\right)\right] J^{p+1}$$

$$\times \left[J^{-1^{p+1}} + \phi^i \Delta t_s \delta_\zeta \left(\frac{\partial \hat{H}^p}{\partial U} - \frac{1}{\mathrm{Re}} \frac{\partial \hat{H}_v^p}{\partial U}\right)\right] \Delta U =$$

$$- \phi^i \Delta t_s \left[J^{-1^{p+1}} \frac{(1+\phi)U^p - (1+2\phi)U^n + \phi U^{n-1}}{\Delta t} - U^p \left(\left(\frac{\xi_t}{J}\right)_\xi + \left(\frac{\eta_t}{J}\right)_\eta + \left(\frac{\zeta_t}{J}\right)_\zeta\right)^{p+1}\right.$$

$$\left. + \delta_\xi \left(\hat{F}^p - \frac{1}{\mathrm{Re}} \hat{F}_v^p\right) + \delta_\eta \left(\hat{G}^p - \frac{1}{\mathrm{Re}} \hat{G}_v^p\right) + \delta_\zeta \left(\hat{H}^p - \frac{1}{\mathrm{Re}} \hat{H}_v^p\right)\right], \tag{13}$$

where

$$\phi^i = \frac{1}{1+\phi}, \qquad \Delta U = U^{p+1} - U^p. \tag{14}$$

For $p = 1$, $U^p = U^n$ and as $p \to \infty$, $U^p \to U^{n+1}$. The numerical scheme reverts to the standard first-order temporal Beam–Warming procedure for $\phi = 0$, $\Delta t_s = \Delta t$, and $p = 1$. In the above expression, the geometric conservation law (GCL)

$$\frac{\partial J^{-1}}{\partial t} + \left(\frac{\xi_t}{J}\right)_\xi + \left(\frac{\eta_t}{J}\right)_\eta + \left(\frac{\zeta_t}{J}\right)_\zeta = 0 \tag{15}$$

has been used to evaluate the term $\partial J^{-1}/\partial t$. This insures satisfaction of the GCL for moving meshes.

With the subiteration approach the right-hand side of equation (13) represents the numerical approximation to the governing equation, while the left-hand side vanishes as $p \to \infty$. The left-hand side, therefore, may be modified without loss of formal accuracy provided a sufficient number of subiterates is employed. In particular, diagonalizing the left-hand side of equation (13) following the approach of Pulliam & Chaussee (1981) improves the efficiency of the algorithm. Although the diagonalized form of the ADI scheme is only first-order time-accurate, when coupled with subiterations, higher-order time accuracy may be recovered (Morton *et al.* 1997). Furthermore, a time step on the left-hand side of the equation Δt_s, may be chosen independently from the physical time step Δt on the right-hand side, thereby enhancing stability. The right-hand side of equation (13) may also be modified to include a higher-order, upwind-biased Roe scheme (Gaitonde, Edwards

& Shang 1995), lagged boundary conditions or lagged turbulence modelling without destroying the implicit nature of the algorithm.

In equation (13), all spatial derivatives are approximated by second-order accurate central differences, and common forms of both implicit and explicit nonlinear dissipation (Jameson, Schmidt & Turkel 1981) are employed in order to preserve numerical stability. The grid speeds x_t, y_t, z_t are computed in a manner consistent with the temporal derivative of the conserved variables in equation (13).

3.2. STRUCTURAL DYNAMICS SOLVER

The structural equations, equations (3)–(5), are solved using standard finite-difference procedures. All spatial derivatives are approximated by using second-order accurate central differences. The temporal derivative is evaluated using Newmark's β method (Humar 1990). In Newmark's β method, the displacement, δw and velocity, $\delta \dot{w}$ are computed using the following relations:

$$\delta \dot{w}^{n+1} = \delta \dot{w}^n + \frac{\Delta t}{2}(\delta \ddot{w}^n + \delta \ddot{w}^{n+1}), \tag{16}$$

$$\delta w^{n+1} = \delta w^n + \Delta t \delta \dot{w}^n + \tfrac{1}{2}(1 - 2\beta)\Delta t^2 \delta \ddot{w}^n + \beta \Delta t^2 \delta \ddot{w}^{n+1}. \tag{17}$$

In the present work, $\beta = \frac{1}{4}$ is used. For this value of β, the scheme reduces to the average acceleration method where the acceleration over an interval is equal to the average of the accelerations at the beginning and end of the interval. This scheme is second-order accurate in time and unconditionally stable.

Substituting the appropriate finite-difference expressions and equation (17) into equations (3)–(5), a set of difference equations is obtained. These equations are solved in an iterative fashion using a Gauss–Seidel solution technique. Equation (3) is uncoupled from equations (4) and (5) by assuming that the membrane stress terms are known when solving this equation. Similarly, in equations (4) and (5), all terms involving δw are assumed to be known when solving these equations. Successive over-relaxation is used with this iterative process in order to accelerate convergence. Convergence is assumed when the change in successive values of δw is less than a specified tolerance.

Coupling of the structural equations with the aerodynamic equations occurs through the surface stress terms, S_{zz}, S_{zx}, S_{zy}, in equations (3)–(5) which result from the aerodynamic forces, and by the resulting deflection of the plate, δw, which is returned to the aerodynamic grid. A simple algebraic method described in Melville *et al.* (1997) deforms the aerodynamic mesh to accommodate the new panel position. In the present numerical scheme, implicit coupling of these two sets of equations is achieved via the previously described subiteration procedure for the aerodynamic equations. By updating the aerodynamic forces in the structural equations and providing the new surface displacement to the aerodynamic solver after each subiteration, the temporal lag between the aerodynamic and structural equations may be eliminated. The importance of this synchronization of the aerodynamic and structural equations will be demonstrated below.

4. BOUNDARY CONDITIONS

The aerodynamic boundary conditions for the panel are as follows. At solid surfaces the no-slip condition is applied, requiring that the fluid velocity at the panel surface should match the surface velocity. The remaining two conditions are the adiabatic wall condition and $\partial p/\partial n = -\rho \mathbf{a}_b \cdot \mathbf{n}$, where $\mathbf{a}_b$ is the acceleration of the body and $\mathbf{n}$ is a vector normal to

the surface. In the inviscid case, the no-slip condition is replaced by a condition assuring that the flow is tangent to the body. At the outflow boundary, all variables are extrapolated from the interior using a first-order extrapolation. Quasi-one-dimensional (1-D) characteristic boundary conditions are applied at all other far-field boundaries.

Boundary conditions for the plate are specified for either pinned edges or for rigidly clamped edges. For either case, no deflection is allowed along the edge of the plate, i.e., $\delta u, \delta v, \delta w = 0$. For pinned edges, the additional condition $\partial^2 \delta w / \partial n^2 = 0$ is specified, which corresponds to no moment on the edge. In the case of a clamped edge, $\partial \delta w / \partial n = 0$ is specified corresponding to zero slope at the edge.

5. RESULTS

The problem to be investigated is the flow over a flexible panel of length a and width b, Figure 1. The response of both semi-infinite panels, $a/b = 0$, and 2-D, square panels, $a/b = 1{\cdot}0$, is studied. Computations are made using both the Euler equations and the full

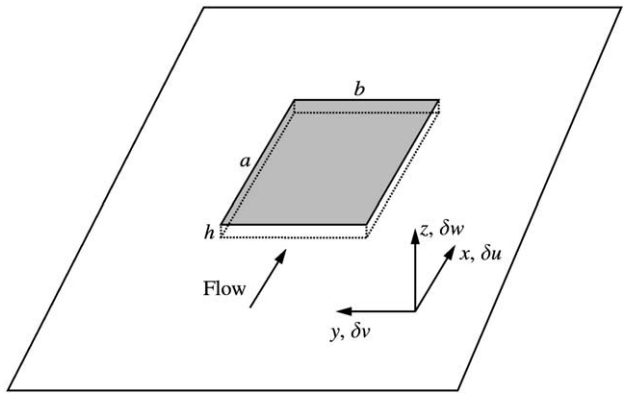

Figure 1. Panel geometry.

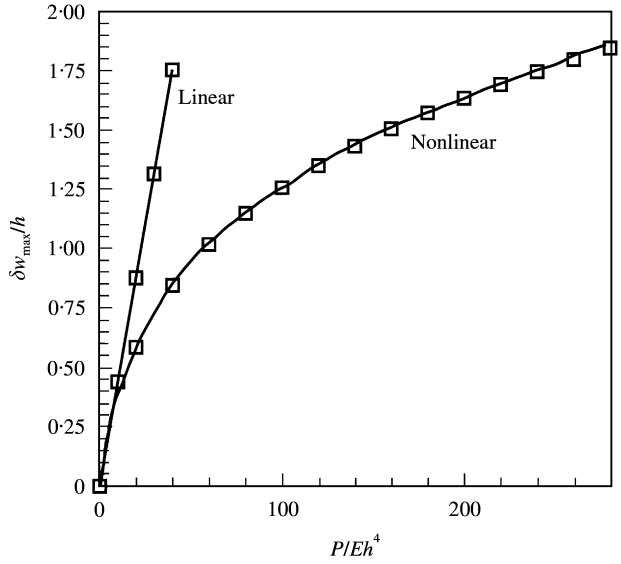

Figure 2. Panel deflection for a uniformly distributed constant load: ——, theory; □, computation.

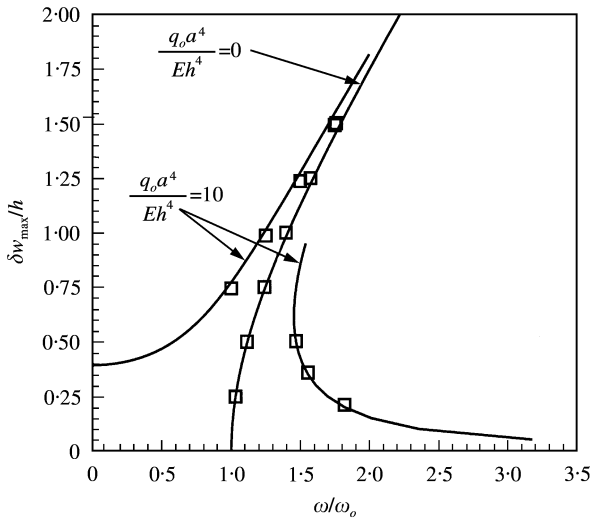

Figure 3. Relationship between forcing frequency and maximum amplitude for a harmonically excited panel: ——, theory; □, computation.

Navier–Stokes equations to explore viscous effects. Unless otherwise noted, the panel has the following properties: thickness $h/a = 0{\cdot}002$, mass ratio $\mu_s = 0{\cdot}1$ and Poisson's ratio $v = 0{\cdot}3$. For all cases freestream pressure, p_∞, is specified on the underside of the panel.

5.1. Structural Solver Validation

The structural solver has been validated for both static and dynamic loads. Figure 2 compares the computed and theoretical (Chia 1980) deflections for a plate subjected to a uniformly distributed load P. Both the linear and nonlinear computed results agree well with the theoretical deflections. From this figure, the importance of the nonlinear effects can be seen. For deflections greater than half the plate thickness, significant deviations between the linear and nonlinear solutions are observed.

Figure 3 presents results for the vibration of a square plate due to a uniformly distributed harmonic forcing function $q_o \cos(\omega t)$. The $q_o = 0$ line represents the free vibration curve. The deviation from the linear free vibration frequency ω_o with increasing vibration amplitude can be seen. Computational and theoretical predictions (Chia 1980) of the free vibration frequency show excellent agreement. Two separate curves are shown for the forcing amplitude, $q_o a^4/Eh^4 = 10$. Curves to the left of the free vibration curve correspond to the driving force and plate response being in phase, while curves to the right of the free vibration curve correspond to the driving force and the plate response being 180° out of phase. The computed and theoretical results again show excellent agreement.

5.2. Two-Dimensional Panel Flutter—Inviscid

The first panel flutter problems computed are for a semi-infinite panel, $a/b = 0$ using the Euler equations. The 2-D case is considered in order to compare with previously existing results of Dowell (1967) using linear potential aerodynamics theory and with Davis (1994) who coupled the Euler equations and a 2-D finite-element solution procedure for the plate. In the present computations, 2-D solutions are obtained with the 3-D code by considering only seven widely spaced ($\Delta y = 10{\cdot}0$) points in the spanwise direction. The panel is free to

deflect at all points in the spanwise direction and the boundary values at the spanwise edges for both the fluids and the structures are obtained by first-order extrapolation from the interior.

The baseline grid for the panel consists of 119 points in the axial direction and 116 points normal to the plate. The grid extends away from the panel 25 plate lengths in all directions; 51 equally spaced points ($\Delta x = 0{\cdot}02$) are located on the panel itself. The minimum spacing at the surface of the panel is $\Delta z = 0{\cdot}001$. A limited study of the effects of grid refinement on the panel has been performed for grids with 26 points ($\Delta x = 0{\cdot}04$) and 101 points ($\Delta x = 0{\cdot}01$) located on the panel. For all computations, the second-order accurate temporal integration scheme for the flow solver is used with a baseline time step $\Delta t = 0{\cdot}02$.

5.2.1. *Supersonic flow*

Flutter computations are first considered for supersonic Mach numbers, $M = 1{\cdot}2$, $1{\cdot}414$ and $1{\cdot}8$. The flutter computations were initiated by providing a small vertical velocity to the first mode of the plate, $\delta\dot{w} = \delta\dot{w}_o \sin(\pi x)$. Figure 4 shows the development of the limit-cycle oscillation for the $M = 1{\cdot}2$ case at a freestream dynamic pressure $\lambda = 100$. Initially, a rapid growth in the amplitude of the oscillations is observed, followed by a levelling off into a limit-cycle flutter response. Figures 5 and 6 plot the variation in flutter amplitude and frequency at the plate location $x/a = 0{\cdot}75$ with freestream dynamic pressure, λ for the differing values of Mach number. In Figure 6, the nondimensional frequency, K_f, is the ratio of the flutter frequency to the fundamental linear frequency of the plate, $\omega_o = \pi^2\sqrt{D/(\rho_s h a^4)}$. Figure 5 compares the computed amplitude variations for $M = 1{\cdot}2$ and $1{\cdot}414$ with the linear, full potential results of Dowell (1967) for pinned boundary conditions. At $M = 1{\cdot}2$, the two solutions show excellent agreement both in flutter onset point and amplitude growth. This is also consistent with the computations of Davis (1994) which showed similar agreement between his Euler solutions and Dowell's results. At the higher Mach number, $M = 1{\cdot}414$, the growth in amplitude for the present computations is consistent with

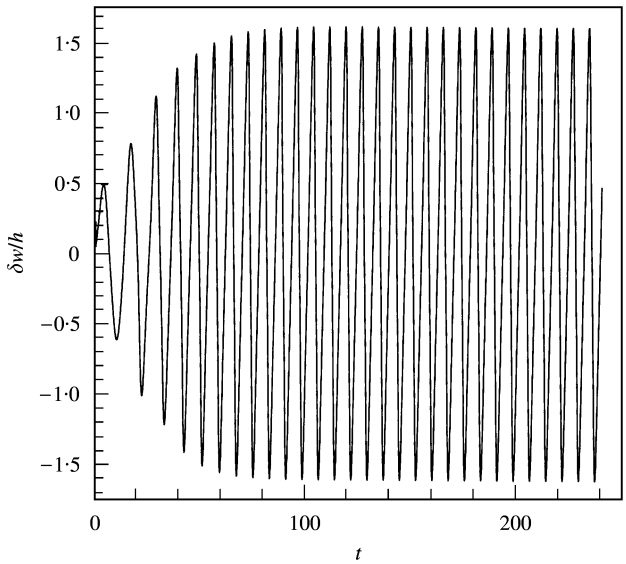

Figure 4. Development of limit cycle at $x/a = 0{\cdot}75$ for $\lambda = 100$ and $M = 1{\cdot}2$.

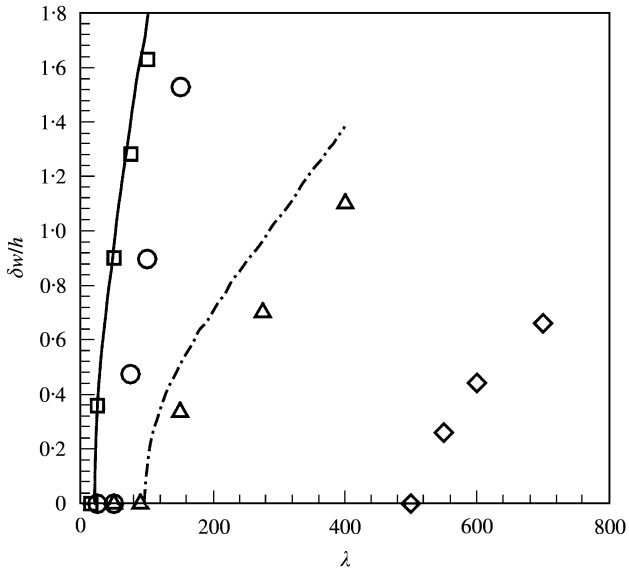

Figure 5. Variation of flutter amplitude with freestream dynamic pressure at $x/a = 0{\cdot}75$: □, $M = 1{\cdot}2$, pinned; ○, $M = 1{\cdot}2$, clamped; △, $M = 1{\cdot}414$, pinned; ◇, $M = 1{\cdot}8$, pinned; ——, Dowell, $M = 1{\cdot}2$; —·—, Dowell, $M = 1{\cdot}414$.

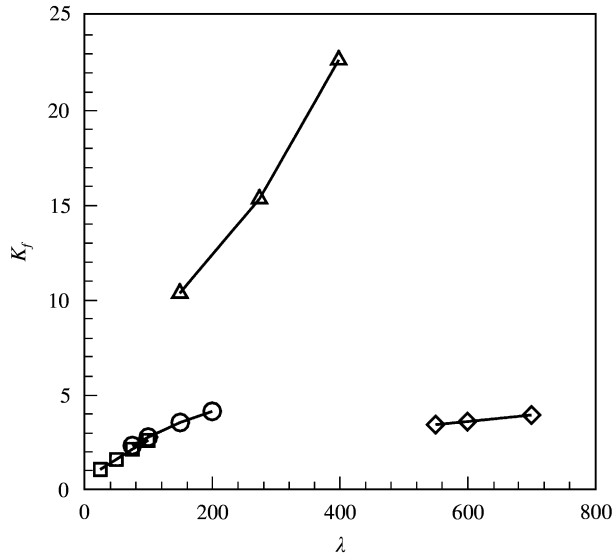

Figure 6. Variation of flutter frequency with freestream dynamic pressure at $x/a = 0{\cdot}75$. —□—, $M = 1{\cdot}2$, pinned; —○—, $M = 1{\cdot}2$, clamped; —△—, $M = 1{\cdot}414$, pinned; —◇—, $M = 1{\cdot}8$, pinned.

Dowell's results but the flutter onset point has shifted to a slightly higher value, due to the nonlinear effects of the Euler flow. This Mach number is in a region where the character of the flutter response changes dramatically (see later discussion) and the flutter onset dynamic pressure is rapidly increasing. It is, therefore, expected that some differences between the present nonlinear Euler computations and the linear results of Dowell (1967) should occur.

The effect of grid resolution is investigated for the $M = 1{\cdot}2$ and $\lambda = 100$ case by repeating this computation on the coarse and fine meshes. The computed results for this case show

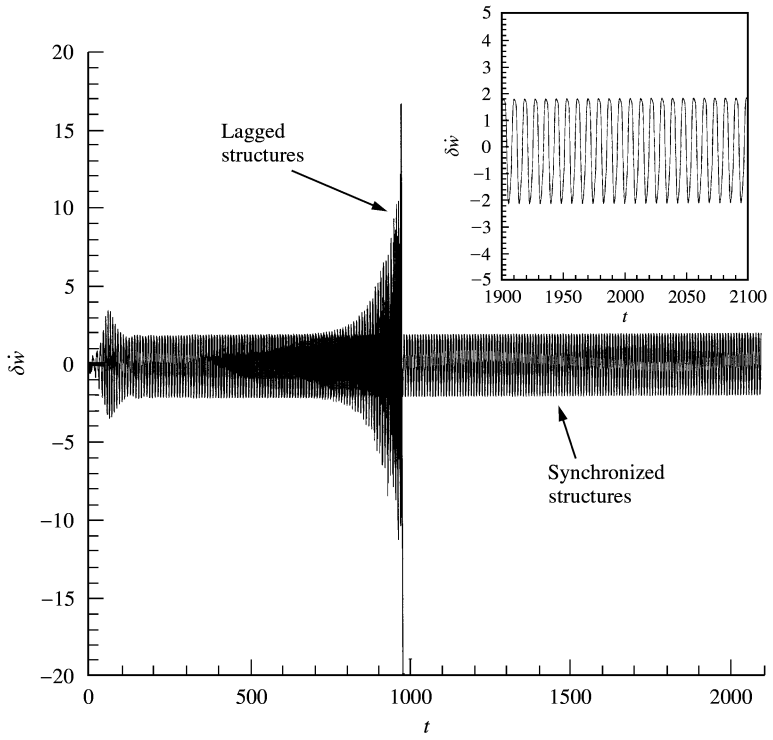

Figure 7. Instability of lagged fluid/structure approach for $M = 1{\cdot}2$, $\lambda = 374$.

little sensitivity to the mesh spacing. On the coarse mesh, the amplitude of the flutter response increases by 0·6% and no discernible change in the frequency is observed. On the fine mesh, the flutter response amplitude decreases by 0·25% and the frequency increases by 0·3%. Since very little difference is observed between the computed results on the three meshes, the baseline mesh is used for all further computations.

As previously discussed, the use of a subiteration strategy in the present numerical scheme allows for synchronization of the aerodynamic and structural formulations. Thus, errors introduced by a lagged fluid/structure coupling approach are eliminated. Figure 7 demonstrates the importance of the implicit coupling of the fluids and structures. In this figure, the time history of the mid-point velocity for the case of lagged structures exhibits a long-time numerical instability. This long-term instability has been observed over a range of Δt values ($0{\cdot}005 \leq \Delta t \leq 0{\cdot}04$). The solution with subiterations exhibits no such behavior, however, even when run for a considerably longer period of time. This spurious behavior of the nonsynchronized approach is believed to be attributable to lagging errors in the aerodynamic/structural coupling and is eliminated quite effectively through the use of subiterations.

The results to this point have all been for pinned boundaries for the plate to facilitate comparison with other work. Other structural boundary conditions may also be computed with the present procedure. In Figures 5 and 6, the effect of employing clamped boundary conditions on all edges of the plate for $M = 1{\cdot}2$ is seen. The primary effect is a slight increase in the flutter dynamic pressure. The growth of the flutter amplitude with increasing dynamic pressure remains similar. The change in boundary condition has very little influence at this Mach number on the frequency of the flutter response.

The Mach number of the flow has a significant effect on the panel flutter response. In Figure 5, the flutter dynamic pressure is seen to increase with higher Mach number. The amplitude of the flutter response decreases with increasing Mach number and the rate of growth of the amplitude also diminishes. The lower values of frequency at the onset of flutter (here taken as the first computed flutter point) for $M = 1{\cdot}2$ and $1{\cdot}8$ are consistent with the flutter onset frequencies reported by Dowell (1967). The frequency of the flutter

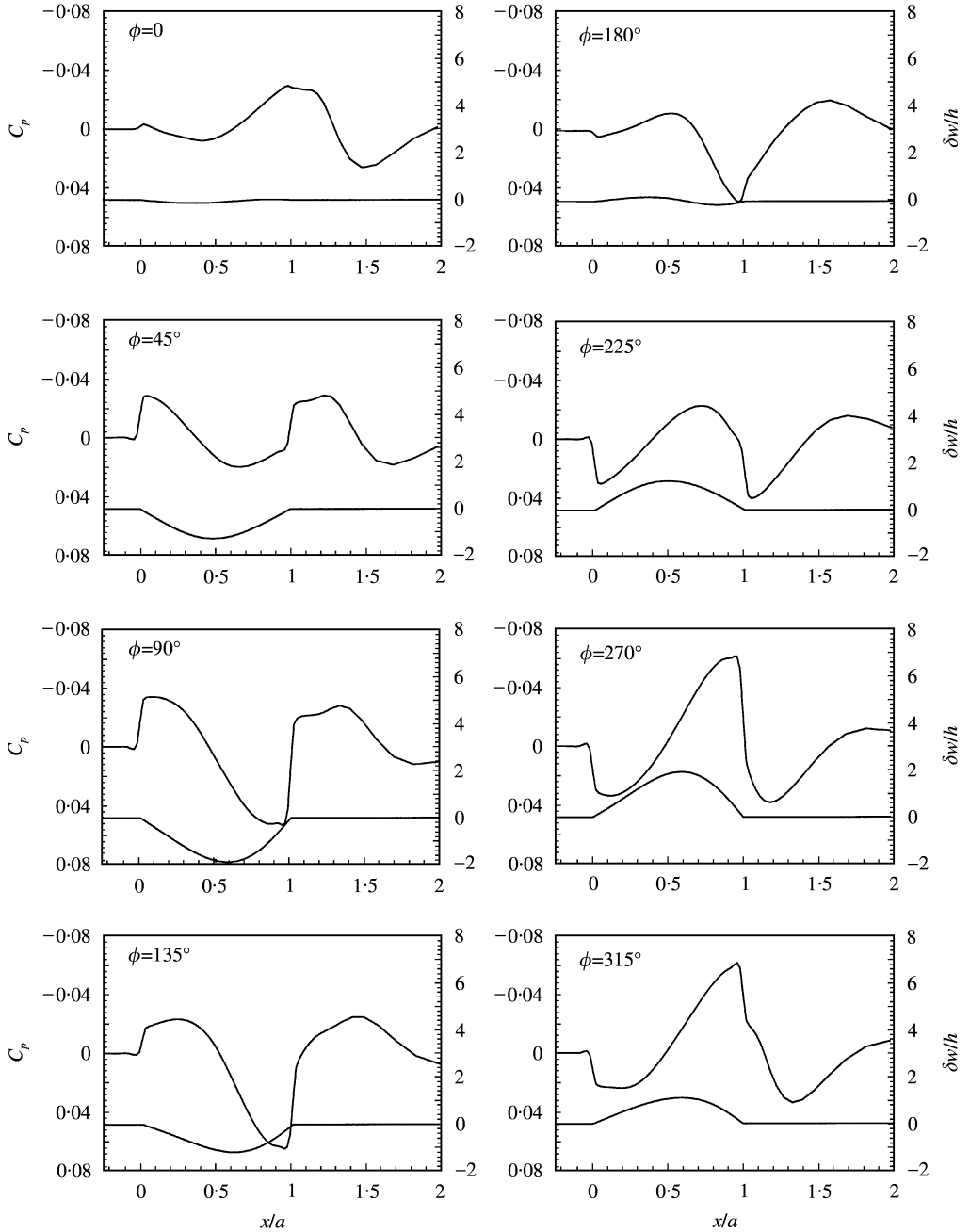

Figure 8. Panel shape and surface pressure during flutter for $M = 1{\cdot}2$, $\lambda = 100$.

response, Figure 6 also shows significant variation with increasing Mach number. The frequency of the response for Mach number $M = 1{\cdot}414$ is notably higher than that for $M = 1{\cdot}2$ and $1{\cdot}8$. Additionally, the frequency at this Mach number shows a steady increase with increasing dynamic pressure.

These results can be better understood by looking at the limit-cycle response at each Mach number. Figure 8 shows one complete cycle of flutter for $M = 1{\cdot}2$ and $\lambda = 100$. The panel deflection occurs primarily in the form of a first mode response with the maximum deflection occurring at $x/a \simeq 0{\cdot}6$. As the panel deflects downward, expansion of the flow around the leading and trailing edges of the plate occurs. Downstream of the plate the flow

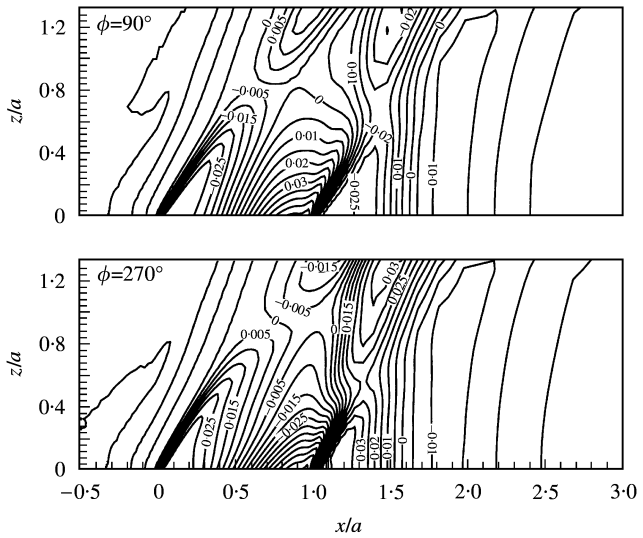

Figure 9. Pressure coefficient contours at the points of minimum and maximum deflection for $M = 1{\cdot}2$, $\lambda = 100$.

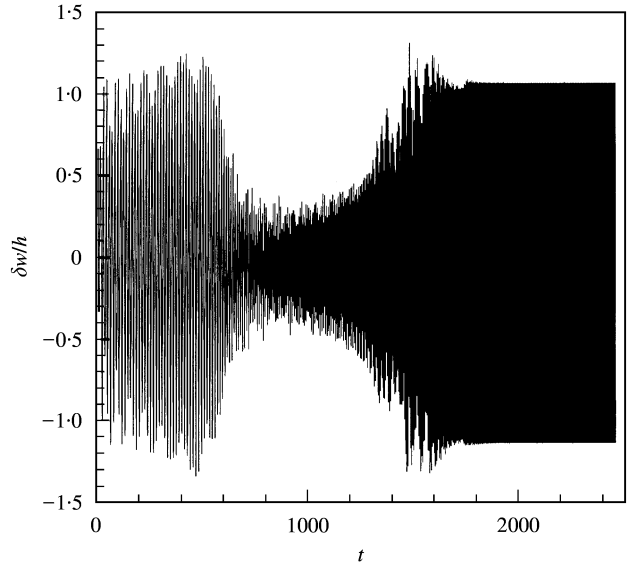

Figure 10. Development of flutter response at $x/a = 0{\cdot}75$ for $M = 1{\cdot}414$, $\lambda = 400$.

recompresses to return to the freestream pressure. As the panel deflects, upward shocks form at the leading and trailing edges with a region of expansion located downstream of the trailing edge of the plate. Figure 9 displays pressure coefficient contours at the minimum and maximum points of deflection. The expansion fans ($\phi = 90^\circ$) and shock waves ($\phi = 270^\circ$); are clearly visible ϕ is the phase angle during the oscillation cycle). Also the pressure disturbances from the fluctuating surface are seen to be propagating along Mach lines as expected.

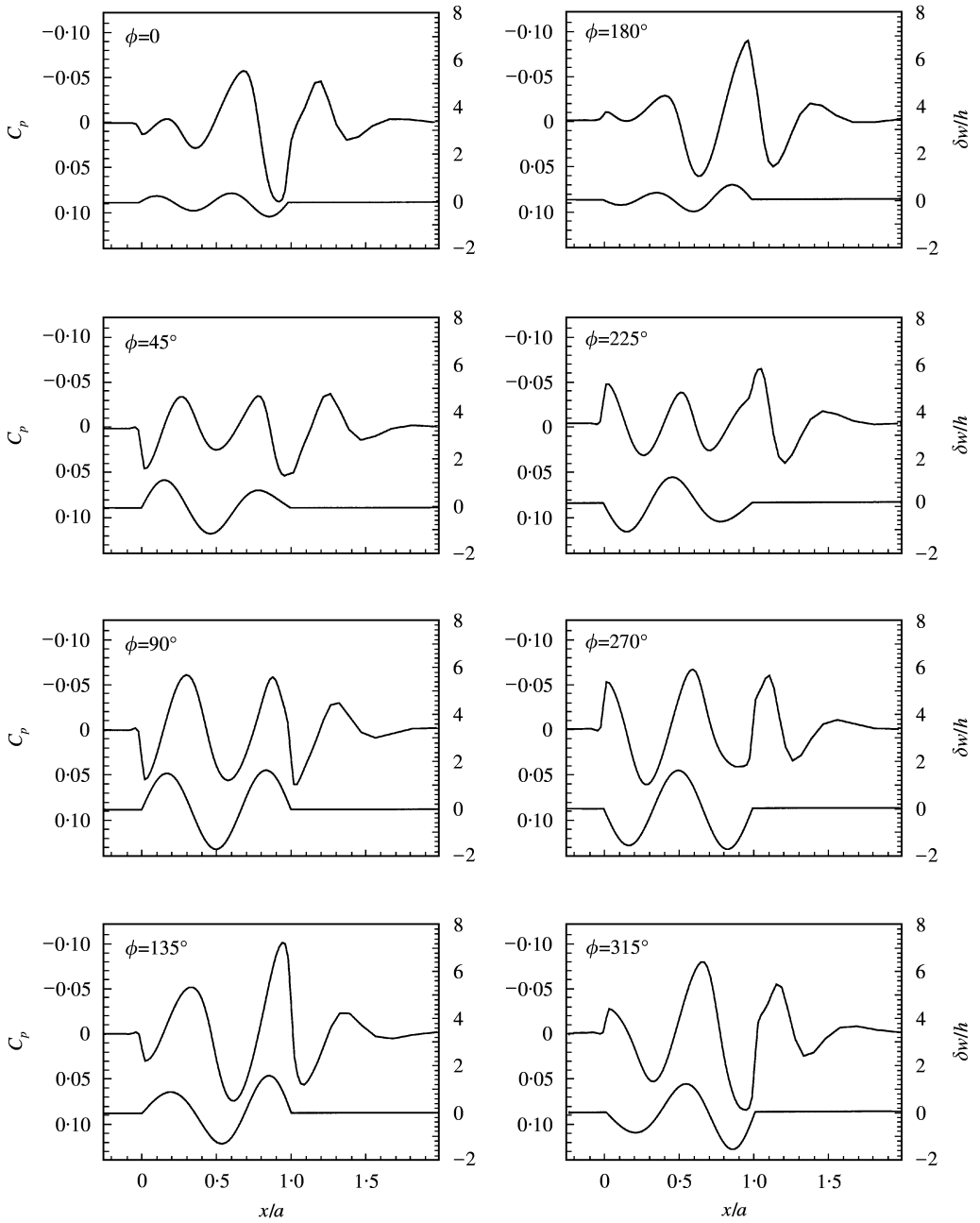

Figure 11. Panel shape and surface pressure during flutter for $M = 1{\cdot}414$, $\lambda = 400$.

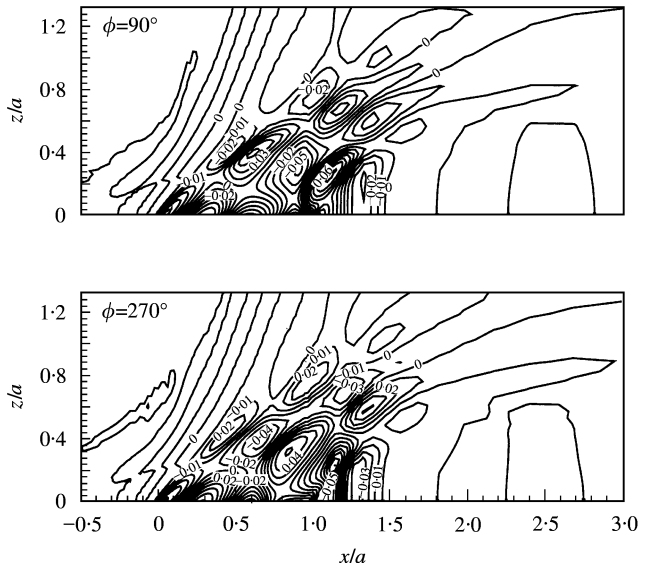

Figure 12. Pressure coefficient contours at the points of minimum and maximum deflection for $M = 1{\cdot}414$, $\lambda = 400$.

At $M = 1{\cdot}414$ considerably longer times were required to establish an asymptotic limit-cycle response for the panel, Figure 10. The reason for this long transient is that the final flutter response at this Mach number involves higher panel modes (predominantly mode 3), Figure 11. Since the flutter response is initiated by a velocity in the first mode, this lower mode response must be damped out. The onset of the higher mode instability then requires further time to grow. This leads to the long transient times required to establish the final flutter response. If the mode participation in the final response could be known *a priori*, these lengthy transients could be reduced by providing an initial velocity in the higher mode. The higher frequency of the response, Figure 6, also results from the fact that the flutter involves higher mode participation. Figure 12 shows a correspondingly more complex pressure field above the panel. Davis (1994) also observed this type of higher mode panel flutter in his Euler computations at $M = 1{\cdot}414$.

As the Mach number is further increased to $M = 1{\cdot}8$, the panel response returns to a lower mode flutter (first mode and second mode participation), Figure 13. Correspondingly, the frequency of the flutter response has dropped to values more commensurate with the $M = 1{\cdot}2$ case. At this Mach number, the frequency remains nearly constant over the range of dynamic pressures considered. The maximum panel deflection occurs further downstream, $x/a \simeq 0{\cdot}75$, than for $M = 1{\cdot}2$. Upstream of $x/a \simeq 0.4$ the deflections of the panel remain quite small. The primary feature seen in the surface pressure is a strong shock or expansion at the trailing edge of the plate. Unlike $M = 1{\cdot}2$, no influence of the panel deflection on the downstream surface pressure is observed. Figure 14 shows the corresponding pressure contours at the points of minimum and maximum deflections. These results indicate that by $M = 1{\cdot}8$ transonic effects are greatly reduced and the solution has the character of supersonic flow.

5.2.2 *Subsonic flow*

Euler computations have also been performed for subsonic freestream Mach numbers, $M = 0{\cdot}9$ and $0{\cdot}95$, for a broad range of freestream dynamic pressures, λ, from very low

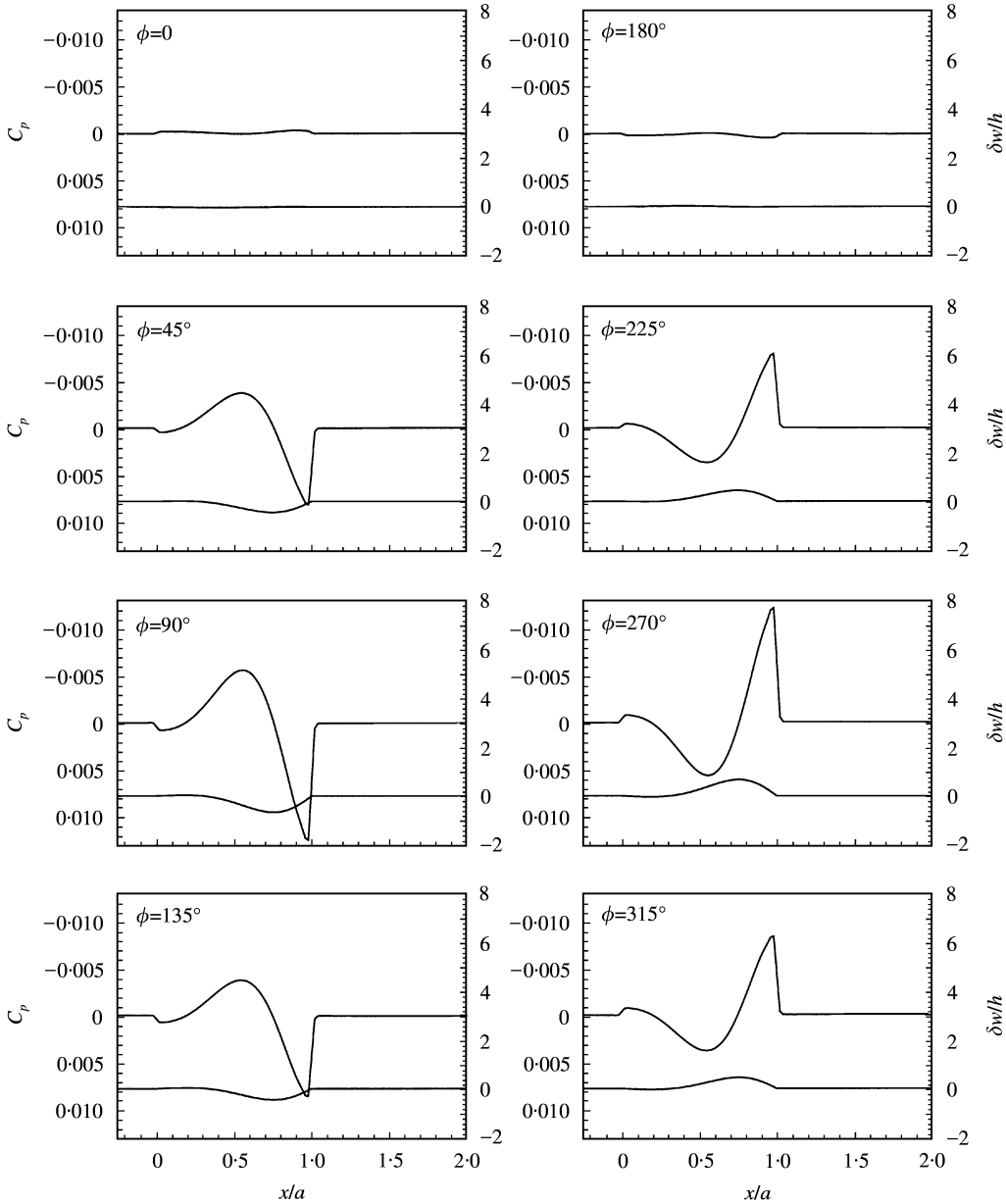

Figure 13. Panel shape and surface pressure during flutter for $M = 1{\cdot}8$, $\lambda = 700$.

values near the onset of panel divergence to values that are significantly larger. At $M = 0{\cdot}9$, two static equilibrium positions for the panel have been found at each value of dynamic pressure over the range considered. One solution consists of an upward deflection of the panel while the other solution consists of a downward deflection of the panel. Figure 15 shows the amplitude of the deflection at the mid-point of the panel as a function of dynamic pressure, λ. The curves for the two solutions are nearly symmetric about the zero deflection line $\delta w/h = 0$. These results are consistent with the classical divergence behavior of a semi-infinite panel as described by Dowell (1975). The initial conditions required to obtain either

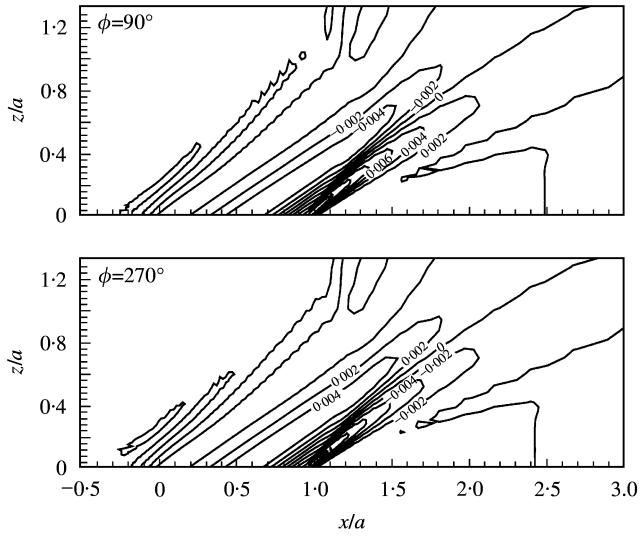

Figure 14. Pressure coefficient contours at the points of minimum and maximum deflection for $M = 1{\cdot}8$, $\lambda = 700$.

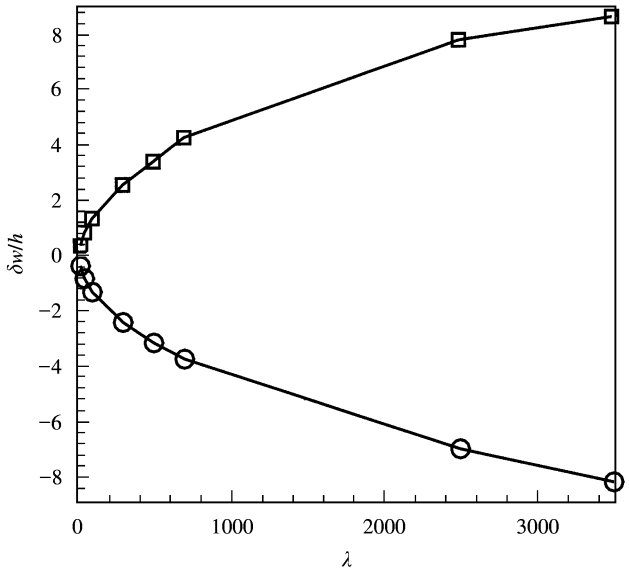

Figure 15. Deflection at the midpoint of the panel, $M = 0{\cdot}9$: –□–, positive deflection; –○–, negative deflection.

the upper or lower solution is a function of the dynamic pressure and the magnitude and direction of the initial velocity given to the plate. At higher values of dynamic pressure ($\lambda = 2500, 3500$) for instance initial velocities in the direction opposite to the final deflected shape were required to obtain that particular solution.

For $M = 0{\cdot}95$, two static equilibrium solutions are obtained for values of dynamic pressure up to $\lambda = 1500$ similar to $M = 0{\cdot}9$, Figure 16. The two solutions at this Mach number are not symmetric about the zero deflection line, however, with the lower solution showing larger deflections at the mid-point of the panel. Figures 17 and 18 display the pressure coefficient contours and panel deflection for the upper and lower solutions,

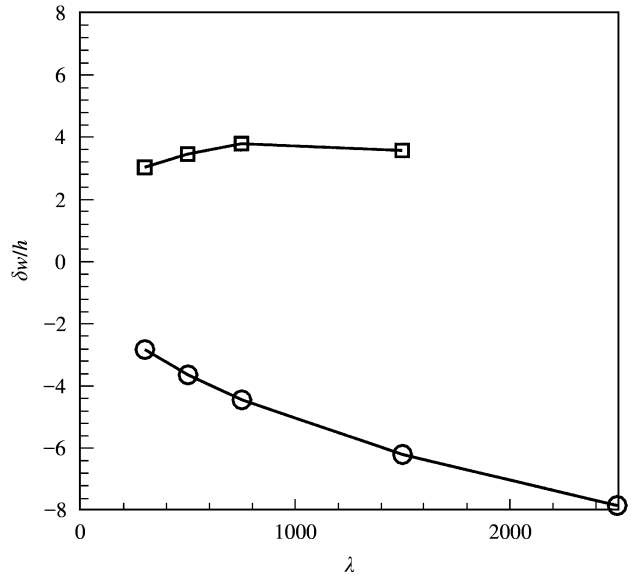

Figure 16. Deflection at the midpoint of the panel, $M = 0{\cdot}95$.—□—, positive deflection; —○—, negative deflection.

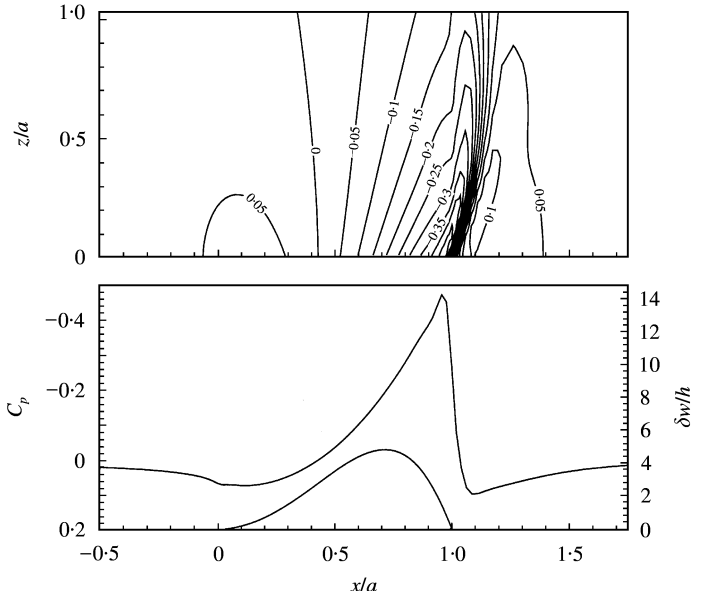

Figure 17. Pressure coefficient contours and panel deflection for the upper solution, $M = 0{\cdot}95$ $\lambda = 1500$.

respectively, for a dynamic pressure, $\lambda = 1500$. The upper solution, Figure 17, shows significant transonic effects with a strong shock wave located at the trailing edge of the panel. This results in a shift of the peak deflection point downstream of the mid-point to $x/a = 0{\cdot}72$. The lower solution, Figure 18, remains more symmetric about the mid-point of the plate. Two weaker shock waves are located just downstream of the leading and trailing edges of the plate.

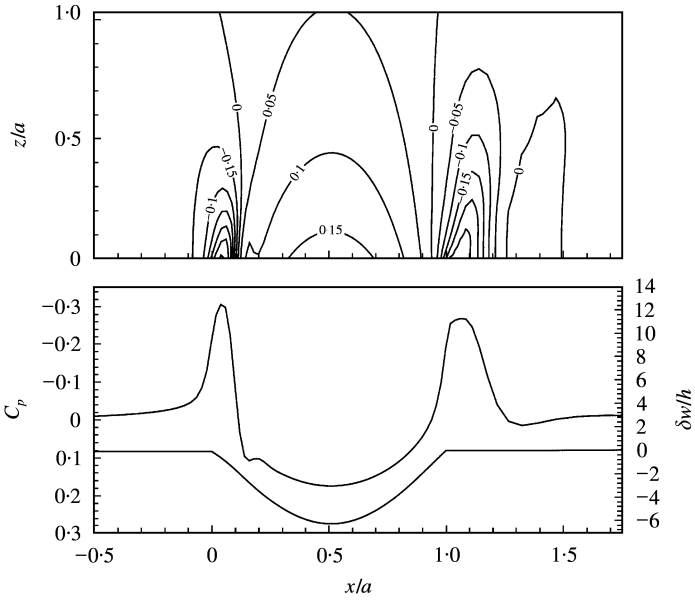

Figure 18. Pressure coefficient contours and panel deflection for the lower solution, $M = 0{\cdot}95$ $\lambda = 1500$.

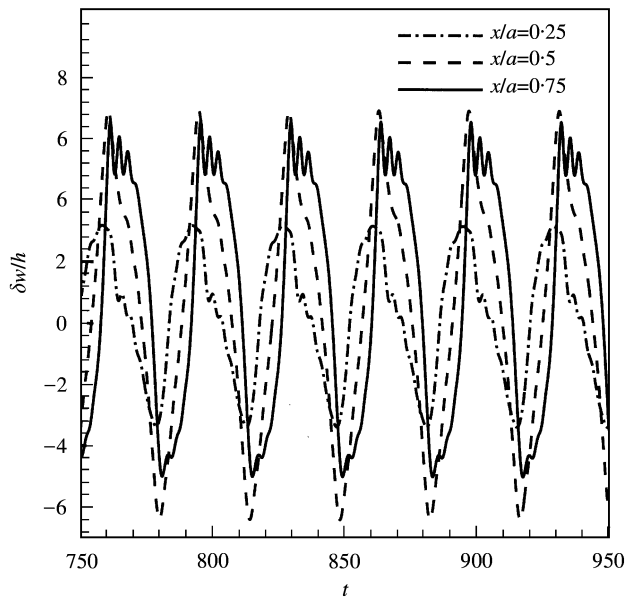

Figure 19. Development of flutter response for $M = 0{\cdot}95$, $\lambda = 2500$.

When the dynamic pressure is raised to a value $\lambda = 2500$, the static downward deflected solution persists. The upper solution becomes unstable, however, and no steady upper solution is obtained. Instead, a flutter solution is found. Figure 19 shows the time histories of the flutter response at three locations on the airfoil. This limit-cycle response is qualitatively similar to one computed by Davis (1994) for similar but not identical flow conditions. The frequency of the flutter response, St = 0·029 is lower than the flutter frequencies at the

supersonic Mach numbers. This complex flutter behavior results from the formation and motion of a shock wave across a significant portion of the length of the panel during one cycle, Figure 20. This shock wave forms initially near the leading edge of the panel at the $\phi = 225^\circ$ point in the cycle, Figure 20. As time progresses the shock strengthens and moves downstream due to the growing upward deflection of the panel. At $\phi = 0$, the shock has strengthened considerably and is located at approximately the mid-point of the panel. The shock continues to move downstream and strengthen until it reaches the trailing edge of the plate, $\phi = 180^\circ$. Once the shock reaches the trailing edge, it remains there and weakens as a new shock is formed upstream and the cycle repeats. One other interesting feature to note

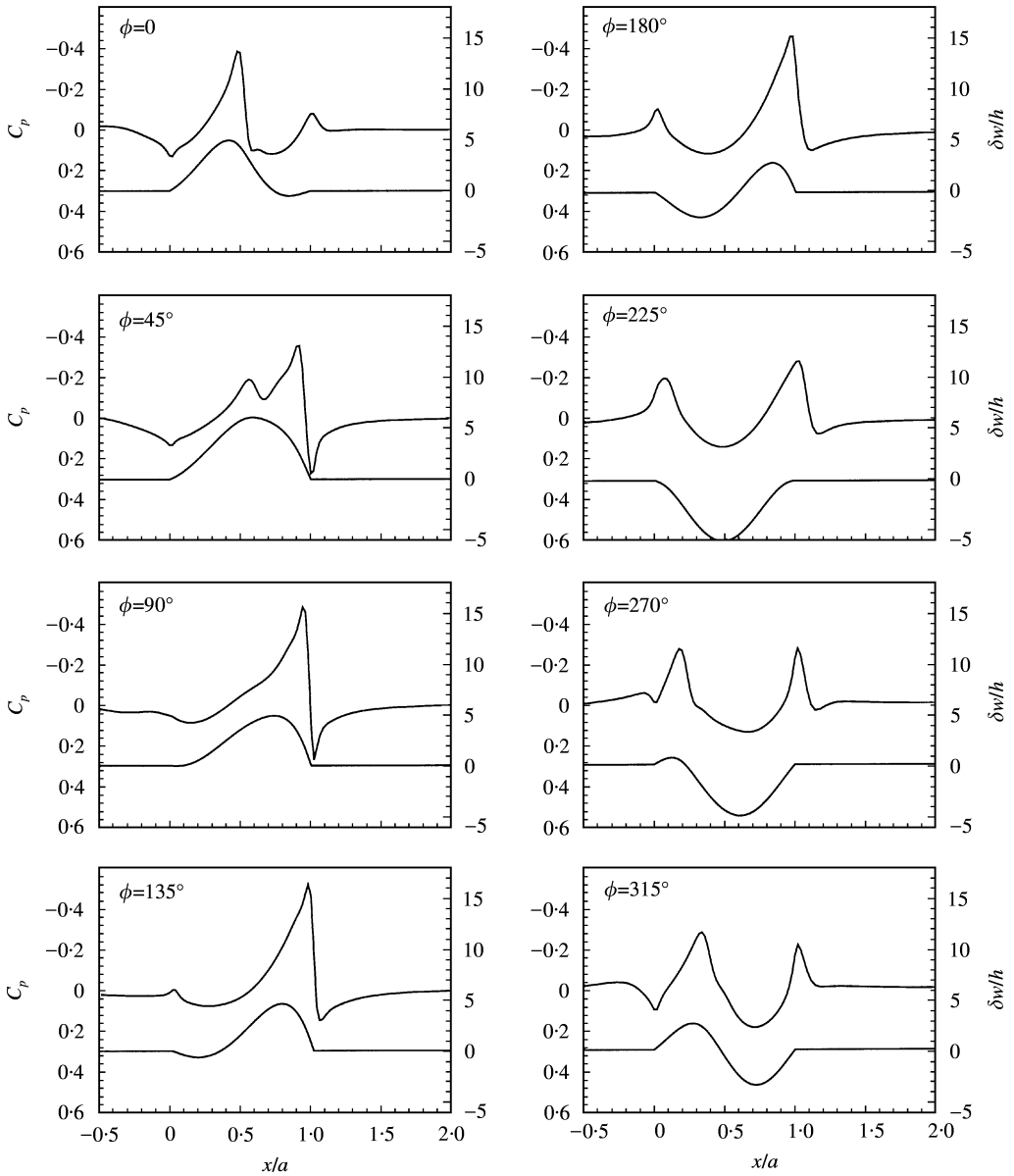

Figure 20. Panel shape and surface pressure during flutter for $M = 0{\cdot}95$, $\lambda = 2500$.

is the development of a double-shock structure at the $\phi = 45^\circ$ point in the cycle. The formation of this second weak shock is a likely contributor to the presence of the high-frequency oscillations at the upper peak of the cycle for $x/a = 0{\cdot}75$, Figure 19.

Computations (not shown here) have also been performed at a Mach number that is just supersonic, $M = 1{\cdot}01$. Multiple solutions were still observed at this Mach number with a stable downward deflected solution and a flutter solution being obtained for a much lower value of dynamic pressure, $\lambda = 75$. At lower values of dynamic pressure only the stable downward deflected solution was obtained. Clearly, very rapid changes in the flutter response are occurring in the region of $M = 1{\cdot}0$.

5.3. Two-Dimensional Panel Flutter—Viscous

The effect of turbulent boundary layers on panel flutter for supersonic Mach numbers has been explored previously by Dowell (1973). In Dowell's work, a shear layer fluid model is used to represent the effects of the boundary layer at high Reynolds number. In the present work, the Navier–Stokes equations are used to provide a more complete model of the viscous aerodynamics. An initial exploration of the effects of viscosity on the flutter of a semi-infinite panel for both subsonic and supersonic flows is performed using this more complex aerodynamic model. For these initial computations, the flow is assumed to be laminar and the Reynolds number is specified as $\mathrm{Re} = 100\,000$ based on the length of the plate, a. The aerodynamic flowfield is modelled using the full Navier–Stokes equations.

5.3.1. *Supersonic flow*, $M = 1{\cdot}2$

Computations at a Mach number $M = 1{\cdot}2$ are performed to explore viscous effects for supersonic flow. For these computations, the upstream boundary of the domain is located at $x/a = -0{\cdot}5$ and a compressible, laminar boundary layer profile is specified as the inflow boundary condition. This allows for direct control of the boundary layer thickness, δ (normalized by the plate length). For each boundary layer thickness considered, an initial solution is computed with no deflection of the plate. An initial velocity is then given to the panel in a similar manner to the Euler flow cases.

Figures 21 and 22 demonstrate the effects of the boundary layer on the amplitude and frequency of the panel flutter at the panel location $x/a = 0{\cdot}75$. Due to the damping effect of the boundary layer, a delay in the onset of flutter and a reduction in the amplitude of the flutter response as compared to the Euler case occurs. Increasing the thickness of the boundary layer further delays the onset of flutter and reduces the rate of growth of both the amplitude and frequency of the flutter response. The frequency at flutter onset increases, however, with increasing boundary layer thickness.

5.3.2. *Subsonic flow*, $M = 0{\cdot}9$

To simplify the treatment of the inflow boundary condition for the subsonic case, the same grid used in the Euler computations is employed and the origin of the boundary layer is specified 2·89 plate lengths upstream of the flexible panel. A flat plate boundary layer is then computed to provide the initial condition for the computations. This results in a boundary layer with a thickness of $\delta = 0{\cdot}04$ at the leading edge of the plate.

As in the inviscid case, two solutions are found for the $M = 0{\cdot}9$ case, an upward deflected solution and a downward deflected solution. Figure 23 shows the static equilibrium upper solution for $M = 0{\cdot}9$ and $\lambda = 450$. The solution is shock-free and the maximum deflection is

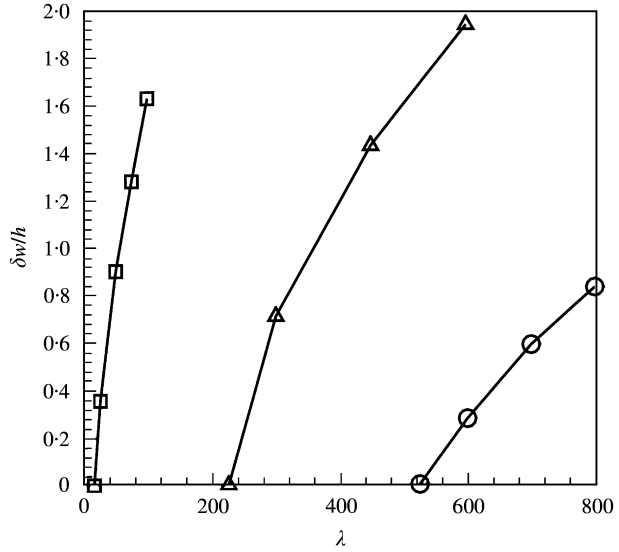

Figure 21. Effect of boundary layer thickness on flutter response amplitude, $M = 1{\cdot}2$: —□—, Euler; —△—, $\delta = 0{\cdot}025$; —○—, $\delta = 0{\cdot}05$.

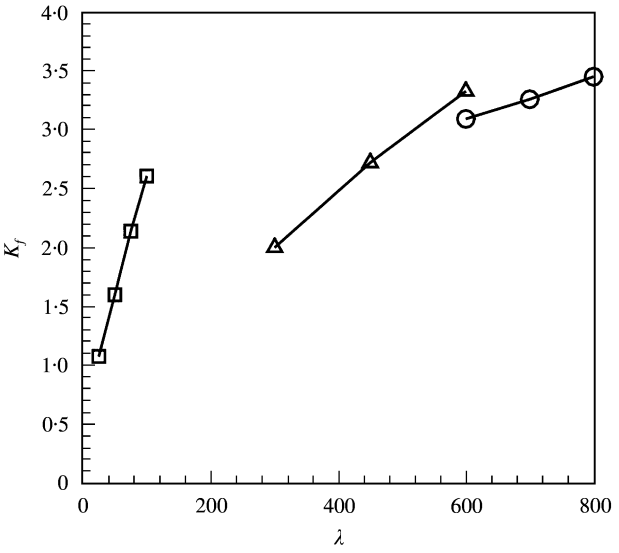

Figure 22. Effect of boundary layer thickness on flutter response frequency, $M = 1{\cdot}2$: —□—, Euler; —△—, $\delta = 0{\cdot}025$; —○—, $\delta = 0{\cdot}05$.

located just downstream of the mid-point of the plate. Figure 24 displays the static equilibrium lower solution for $M = 0{\cdot}9$ and at a lower value of dynamic pressure $\lambda = 300$. In each case, the amplitude of the deflection at the mid-point of the panel is less than in the inviscid case, Figure 15.

When the freestream dynamic pressure is raised to a value $\lambda = 450$, the lower solution undergoes a very interesting transformation, Figure 25. Initially, the solution appears to converge to a new static equilibrium position. As time progresses, however, an instability develops and a small amplitude flutter solution is obtained. As energy is transferred to this

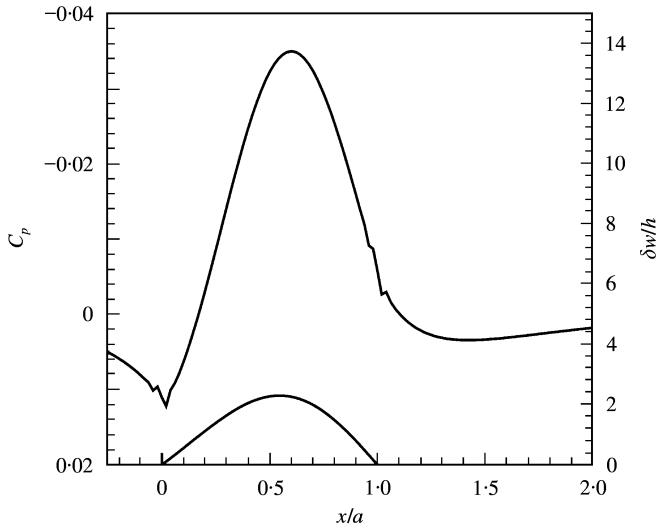

Figure 23. Viscous upper solution for $M = 0{\cdot}9$, $\lambda = 450$.

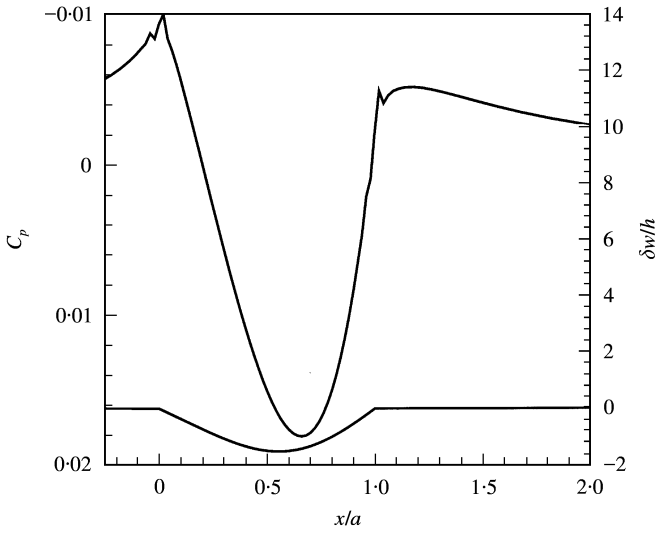

Figure 24. Viscous lower solution for $M = 0{\cdot}9$, $\lambda = 300$.

new flutter solution, the mean deflection of the panel is reduced. This flutter differs from the previously described flutter behavior because the panel oscillations are occurring about a mean deflected position. The frequency of the oscillations are high, St = 1·61 ($K_f = 68{\cdot}8$).

Figure 26 shows the instantaneous panel shape and the surface pressure at the point of maximum upward deflection at $x/a = 0{\cdot}75$. The panel deflection appears to consist of a mean first-mode deflection with a higher frequency (mode 8), low-amplitude deflection superimposed on top. This results in high-frequency spatial oscillations in the surface pressure distribution. As time progresses, these waves along the panel surface oscillate about the mean deflected position.

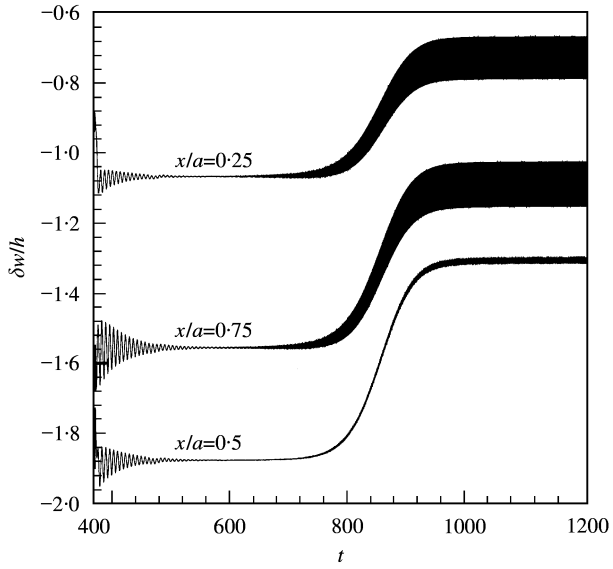

Figure 25. Temporal development of flutter for the lower solution, $M = 0{\cdot}9$, $\lambda = 450$.

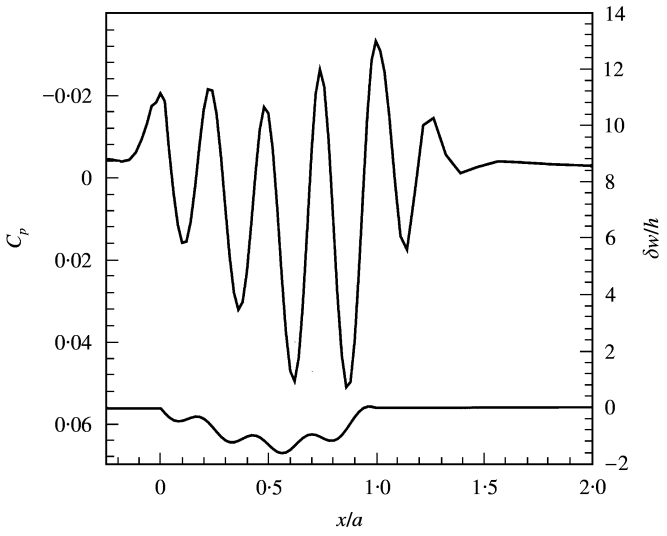

Figure 26. Instantaneous panel shape and surface pressure, $M = 0{\cdot}9$, $\lambda = 450$.

The corresponding instantaneous pressure contours and vorticity contours in the boundary layer are shown in Figures 27(a) and 28(a). In Figure 28, the distance normal to the surface has been magnified by a factor of 8 to better visualize the results. The panel motion produces the radiation of acoustic waves from the moving surface, Figure 27(a). Strong vorticity waves are also seen in the boundary layer, Figure 28(a).

In order to determine whether the present panel motion is being driven solely by an instability of the boundary layer, the panel was fixed at its deflected position, Figure 26. The solution rapidly converged to the steady solution seen in Figures 27(b) and 28(b). The acoustic waves observed in Figure 27(a) are no longer present and the vorticity waves in the boundary layer are greatly diminished, Figure 28(b), indicating no boundary layer

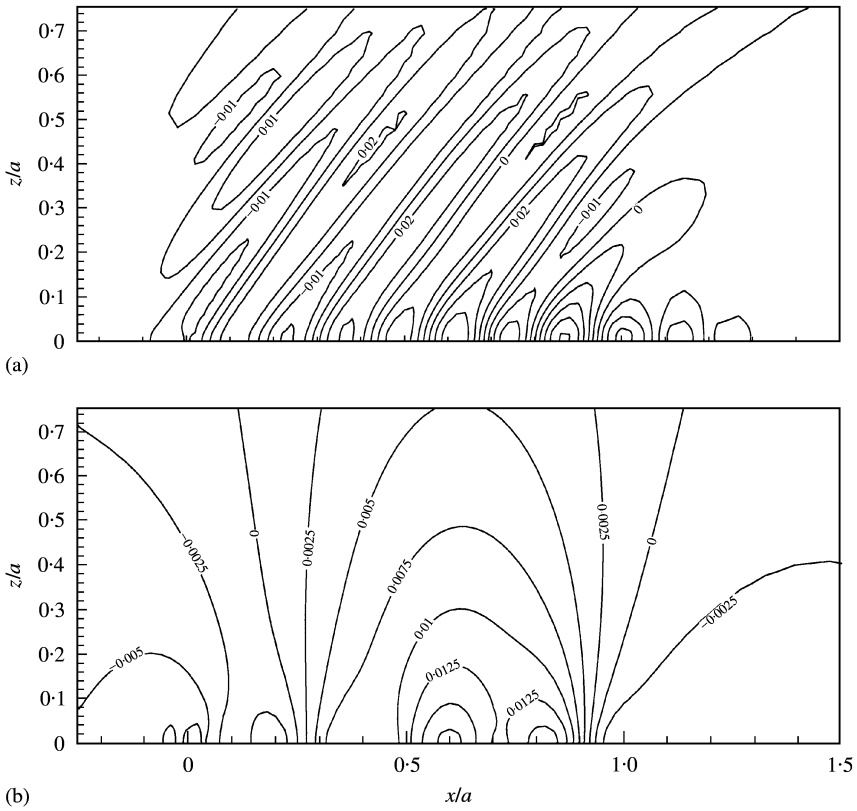

Figure 27. Pressure coefficient contours, $M = 0{\cdot}9$, $\lambda = 450$ (a) flexible structure; (b) fixed (rigid) structure.

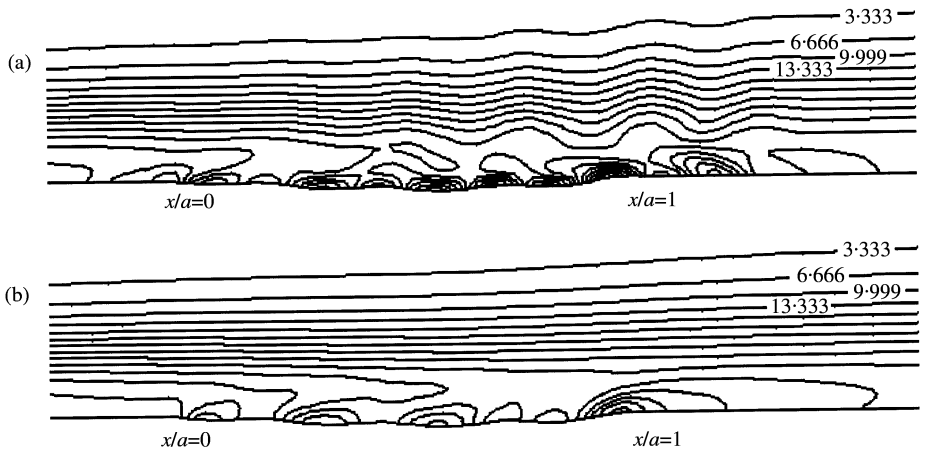

Figure 28. Vorticity contours, $M = 0{\cdot}9$, $\lambda = 450$: (a) flexible structure; (b) fixed structure.

instability in the absence of panel motion. Coupling this fact with the observation that no similar flutter behavior occurs for the inviscid case demonstrates that this flutter phenomena results from a true fluid/structure interaction between the flexible panel and the viscous flow above the panel.

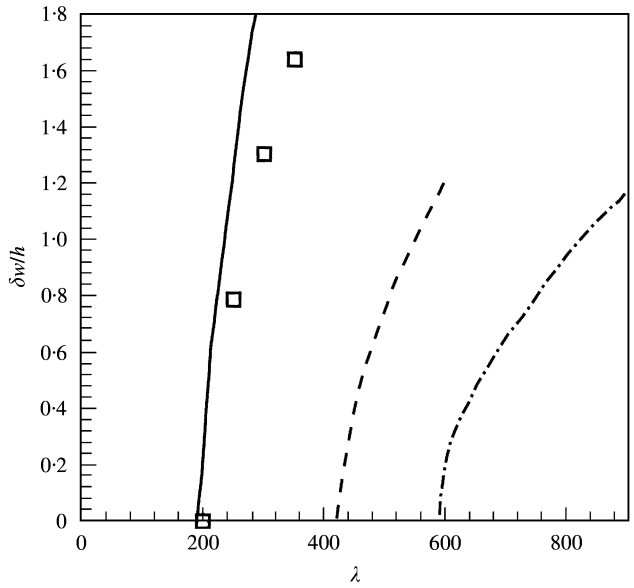

Figure 29. Limit-cycle amplitude versus dynamic pressure for three-dimensional panel flutter: □, $M = 1{\cdot}2$, pinned; ——, Dowell, $M = 1{\cdot}2$; – – – –, Dowell, $M = 1{\cdot}414$; – · – · – · –, Dowell, $M = 1{\cdot}6$.

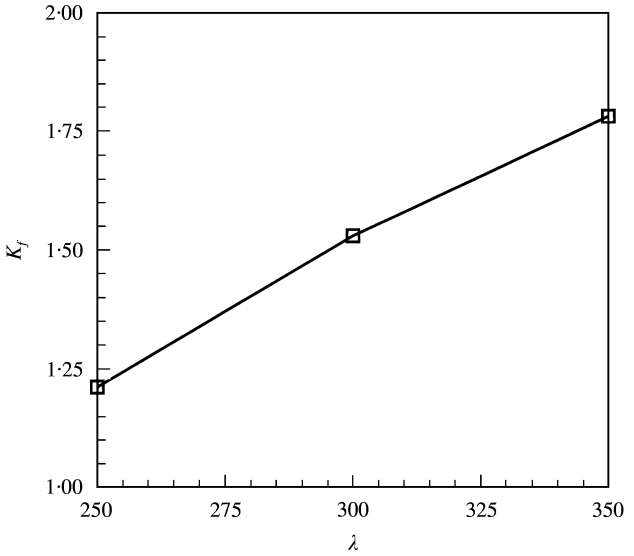

Figure 30. Limit-cycle frequency versus dynamic pressure for three-dimensional panel flutter.

Further computations were performed to observe whether this flutter behavior persists. The flutter behavior of the lower solution was seen to remain for values of dynamic pressure up to $\lambda = 750$. Higher values of dynamic pressure were not considered. The thickness of the panel was also doubled to $h/a = 0{\cdot}004$ but the observed flutter behavior remained. Viscous computations at a higher Mach number, $M = 0{\cdot}95$, also exhibited this flutter behavior for the lower solution. Finally, the same flutter behavior has been reproduced by Visbal

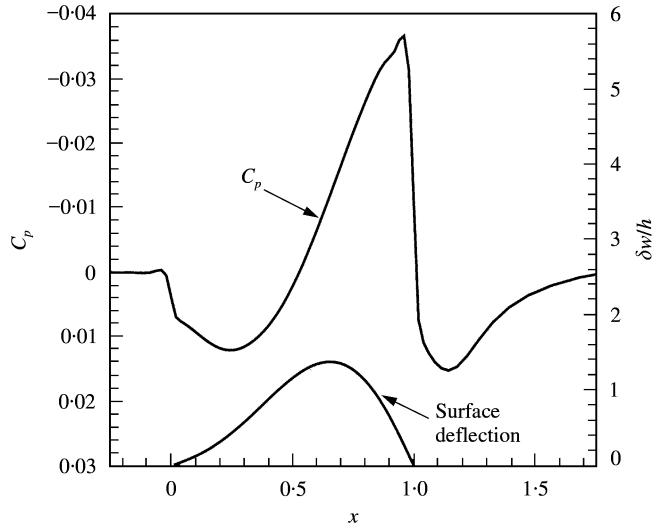

Figure 31. Surface pressure and deflection for $M = 1{\cdot}2$, $\lambda = 300$ at peak upward deflection.

& Gordnier (2001) using a higher-order (sixth order) compact scheme for the aerodynamic solver.

5.4. Three-Dimensional Panel Flutter—Inviscid

Initial computations for 3-D panel flutter are performed for a square panel, $a/b = 1{\cdot}0$. Both supersonic, $M = 1{\cdot}2$, and subsonic, $M = 0{\cdot}95$ Mach numbers are considered. The grid for the 3-D mesh is obtained by using the same grid distributions employed in the 2-D case with the spanwise distribution being the same as the axial direction. Figures 29 and 30 present the variation of the limit-cycle amplitude and frequency at a point on the center-line of the plate and at a location $x/a = 0{\cdot}75$ for $M = 1{\cdot}2$. For a 2-D panel, the fundamental linear frequency is given by the expression $\omega_o = \pi^2(1 + \mathrm{AR}^2)\sqrt{D/(\rho_s h a^4)}$, where $\mathrm{AR} = a/b$ is the panel aspect ratio. The computed results at $M = 1{\cdot}2$ again show reasonable agreement with the linearized potential results of Dowell (1967) both in the amplitude of the response and the frequency at flutter onset. Some small discrepancies are observed at higher amplitudes which may be attributable to the use of the Euler equations for the aerodynamic model in the present computations.

Figure 31 shows the panel surface deflection and surface pressure at a point in the limit cycle of maximum upward deflection for the conditions $M = 1{\cdot}2$ and $\lambda = 300$. The surface deflection is predominantly in the first mode with the point of maximum deflection located at $x/a = 0{\cdot}66$. The surface pressure exhibits a weak shock at the leading edge of the panel and a stronger shock at the trailing edge. Figures 32 and 33 display contours of the surface pressure coefficient and surface deflection at the same instant. The results are seen to be symmetric about the centerline, $y/a = 0{\cdot}5$, and exhibit significant spanwise variation in pressure. The shocks are strongest along the centerline of the plate and weaken towards the edges $y/a = 0{\cdot}0$ and $1{\cdot}0$, where the deflection of the plate is reduced.

Three-dimensional computations have also been performed for a subsonic Mach number $M = 0.95$ and dynamic pressure $\lambda = 500$. For this value of dynamic pressure two solutions are obtained, Figure 34. Figure 34(a, b) shows the case in which the panel is deflected in an

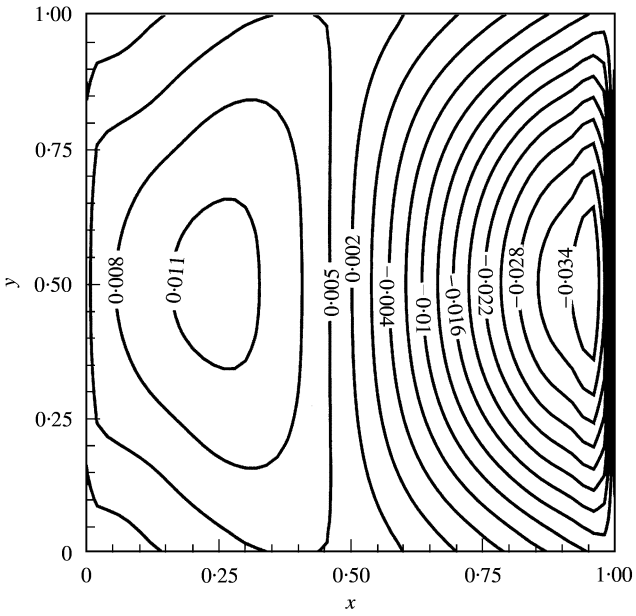

Figure 32. Surface pressure contours for $M = 1{\cdot}2$, $\lambda = 300$ at peak upward deflection.

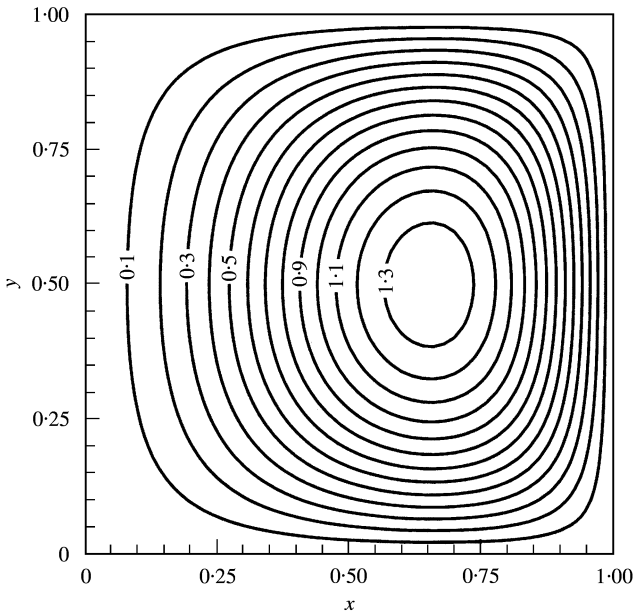

Figure 33. Surface deflection, $\delta w/h$ for $M = 1{\cdot}2$, $\lambda = 300$ at peak upward deflection.

upward direction. Figure 34(c, d) displays results for the same conditions but with the plate deflected in a downward direction. In each case, the solutions are again symmetric about the spanwise center-line. These results are similar to the multiple solutions observed for the semi-infinite panel at subsonic Mach numbers. Computations of higher dynamic pressures, where the upper solution became unstable, have not yet been computed and are a source for further investigation.

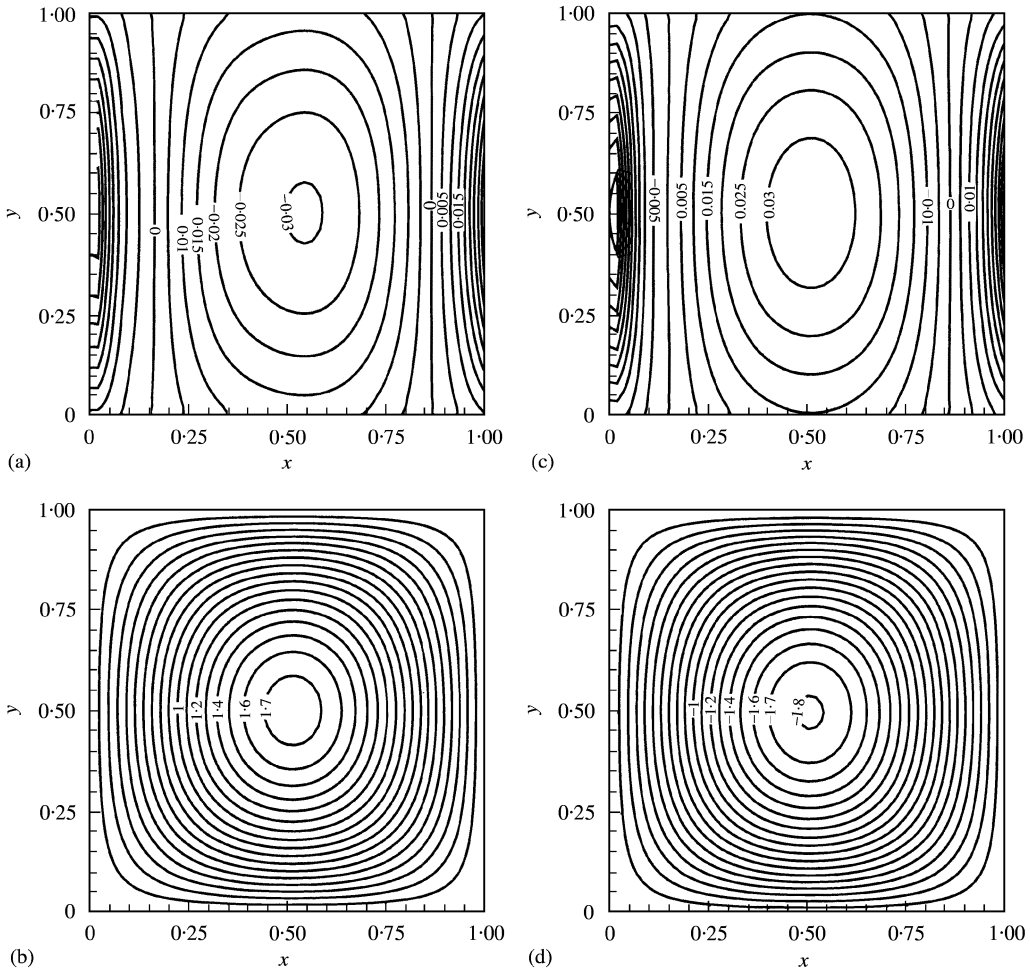

Figure 34. (a, c) Pressure coefficient contours and (b, d) surface deflection; (a, b) for the upper and (c, d) lower solutions at $M = 0{\cdot}95$, $\lambda = 500$.

6. CONCLUSIONS

A 3-D aeroelastic solver for high fidelity simulations of nonlinear panel flutter has been developed. The solution procedure couples a full Navier–Stokes solver with a finite-difference solver for the von Karman plate equations. Several classical plate problems have been used to validate the structural solver. An innovative subiteration strategy provided synchronization between the fluid and structures. The importance of eliminating errors resulting from the lagging of the structural solver has been demonstrated for the panel flutter problem.

This new solution scheme has been applied to the computation of inviscid, 2-D, panel flutter for subsonic and supersonic Mach numbers. The supersonic flow cases showed good agreement with the earlier works of Dowell (1967) and Davis and Bendiksen (Davis &, Bendiksen 1993; Davis 1994). For subsonic flows two solutions were obtained, a static upward deflection of the panel and a static downward deflection of the panel. At $M = 0{\cdot}95$

and higher values of freestream dynamic pressure, the upper solution becomes unstable and a complex flutter behavior dominated by large shock motions across the panel is obtained.

The effects of viscosity on the 2-D panel flutter were also investigated. For supersonic Mach numbers, the presence of the boundary layer delayed the onset of flutter to higher values of dynamic pressure. The frequency of the oscillations was also reduced. At subsonic Mach numbers, two solutions were seen to exist as in the inviscid case. As the dynamic pressure was increased, the lower solution branch exhibited an interesting new flutter behavior. This small amplitude flutter behavior consisted of a mean first mode deflection with oscillations in a higher mode (mode 8) occurring about this mean position. This behavior was shown to result from a true coupling between the flexible panel and the viscous flow above the panel. The motion of the panel produces the radiation of acoustic pressure waves away from the panel surface.

Initial computations for 3-D panel flutter have also been completed for inviscid supersonic and subsonic flows. The supersonic flow results for $M = 1{\cdot}2$ show reasonable agreement with the previous work of Dowell (1967). Multiple solutions for the subsonic case were also observed in the 3-D computations with static upward deflected and static downward deflected solutions obtained.

ACKNOWLEDGEMENT

The authors are grateful for AFOSR sponsorship under task 2304IW monitored by Dr L. Sakell. This work was also supported in part by a grant of HPC time from the DoD HPC Shared Resource Centers at ARL and NAVO.

References

Abdel-Motaglay, K., Chen, R. & Mei, C. 1999 Nonlinear flutter of composite panels under yawed supersonic flow using finite elements. *AIAA Journal* **37,** 1025–1032.

Beam, R. M. & Warming, R. F. 1978 An implicit factored scheme for the compressible Navier–Stokes equations. *AIAA Journal* **16,** 393–402.

Bendiksen, O. & Davis, G. 1995 Nonlinear traveling wave flutter of panels in transonic flow. Paper AIAA-95-1486.

Bendiksen, O. & Hwang, G. 1997 Nonlinear flutter calculations for transonic wings. CEAS Forum on Aeroelasticity and Structural Dynamics, Rome, Italy.

Chia, C. 1980 *Nonlinear Analysis of Plates*. New York: McGraw-Hill.

Davis, G. A. 1994 Transonic aeroelasticity solutions using finite elements in an arbitrary Lagrangian–Eulerian formulation. Ph.D. Dissertation, Department of Aerospace Engineering, University of California Los Angeles, Los Angeles, CA, U.S.A.

Davis, G. & Bendiksen, O. 1993 Transonic panel flutter. Paper AIAA-93-1476.

Dowell, E. H. 1966 Nonlinear oscillations of a fluttering plate. *AIAA Journal* **4**, 1267–1275.

Dowell, E. H. 1967 Nonlinear oscillations of a fluttering plate. II. *AIAA Journal* **5**, 1856–1862.

Dowell, E. H. 1970 Panel flutter: a review of the aeroelastic stability of plates and shells. *AIAA Journal* **8**, 385–399.

Dowell, E. H. 1973 Aerodynamic boundary layer effects on flutter and damping of plates. *Journal of Aircraft* **10**, 734–738.

Dowell, E. H. 1975 *Aeroelasticity of Plates and Shells*. Leyden: Noordhoff International Publishing.

Fung, Y. C. 1965 *Foundations of Solid Mechanics*. Englewood Cliffs, NJ: Prentice-Hall.

Gaitonde, D., Edwards, J. & Shang, J. 1995 The computed structure of a 3-D turbulent interaction caused by a cylinder/offset flare juncture. Paper AIAA-95-0230.

Gordnier, R. E. & Melville, R. B. 1998 Accuracy issues for transonic wing flutter using 3-D Navier–Stokes. Paper AIAA-98-1729.

Gordnier, R. E. & Melville, R. B. 1999 Physical mechanisms for limit-cycle oscillations of a cropped delta wing. Paper AIAA-99-3796.

GORDNIER, R. E. & VISBAL, M. R. 1991 Numerical simulation of the unsteady vortex structure over a delta wing. Paper AIAA-91-1811.
GURUSWAMY, G. P. 1990 Unsteady aerodynamic and aeroelastic calculations for wings using Euler equations. *AIAA Journal* **28**, 461–469.
HUMAR, J. L. 1990 *Dynamics of Structures.* Englewood Cliffs, NJ: Prentice-Hall.
JAMESON, A., SCHMIDT, W. & TURKEL, E. 1981 Numerical solutions of the Euler equations by finite volume methods using Runge–Kutta time-stepping schemes. Paper AIAA-81-1259.
MELVILLE, R. B., MORTON, S. A. & RIZZETTA, D. P. 1997 Implementation of a fully-implicit, aeroelastic Navier-Stokes solver. Paper AIAA-97-2039.
MORTON, S. A. & BERAN, P. S. 1995 Nonlinear analysis of airfoil flutter at transonic speeds. Paper AIAA-95-1905.
MORTON, S. A., MELVILLE, R. B. & VISBAL, M. R. 1997 Accuracy and coupling issues of aeroelastic Navier–Stokes solutions on deforming meshes. Paper AIAA-97-1085.
MORTON, S. A., RIZZETTA, D. P. & MELVILLE, R. B. 1998 Numerical simulation of the interaction between a leading-edge vortex and a flexible vertical tail. Paper AIAA-98-1957.
PULLIAM, T. H. & CHAUSSEE, D. S. 1981 A diagonal form of an implicit approximate-factorization algorithm. *Journal of Computational Physics* **39**, 347–363.
PULLIAM, T. H. & STEGER, J. L. 1980 Implicit finite-difference simulation of three-dimensional compressible flows. *AIAA Journal* **18**, 159–167.
RIZZETTA, D. P. & VISBAL, M. R. 1992 Comparative numerical study of two turbulence models for airfoil static and dynamic stall. Paper AIAA-92-4649.
SELVAM, R., VISBAL, M. R. & MORTON, S. A. 1998 Computation of nonlinear viscous panel flutter using a fully implicit aeroelastic solver. Paper AIAA-98-1844.
VISBAL, M. R. & GORDNIER, R. E. 2000 A high-order flow solver for deforming and moving meshes. Paper AIAA-2000-2619.

APPENDIX:NOMENCLATURE

AR	aspect ratio, a/b
a	plate length
b	plate width
C_p	pressure coefficient
D	plate stiffness, $E_s h^3/12(1-\nu^2)$
E	total specific energy
E_s	Young's modulus
$\hat{F}, \hat{G}, \hat{H}$	inviscid vector fluxes
$\hat{F}_v, \hat{G}_v, \hat{H}_v$	viscous vector fluxes
h	plate thickness
J	transformation Jacobian
K_f	nondimensional frequency, ω/ω_0
M	freestream Mach number
N'_x, N'_y, N'_z	membrane stresses
p	pressure
Re	Reynolds number, $\mathrm{Re} = \rho_\infty u_\infty a/\mu_\infty$
S_{zz}, S_{zx}, S_{zy}	Kirchhoff stress tensor components
St	Strouhal number, $\mathrm{St} = fa/u_\infty$
t	nondimensional time $t = \bar{t}u_\infty/a$
u, v, w	velocity components in x, y and z
x, y, z	physical coordinates
β	Newmark's β constant, $\beta = 0{\cdot}25$
$\delta u, \delta v, \delta w$	structural displacements
λ	dynamic pressure, $\rho_\infty u_\infty^2 a^3/D$
μ	viscosity coefficient

μ_s	mass ratio, $\rho_\infty a/\rho_s h$
ξ, η, ζ	computational coordinates
ρ	density
ρ_s	structural mass density
ϕ	phase angle during oscillation cycle
ω	circular frequency
ω_0	linear free vibration circular frequency
$(\dot{})$	time differentiation